Hindawi
International Journal of Rotating Machinery
Volume 2020, Article ID 9540791, 13 pages
https://doi.org/10.1155/2020/9540791

Research Article

Application of Axis Orbit Image Optimization in Fault Diagnosis for Rotor System

Xinyu Pang,[1,2] **Jie Shao**,[3] **Xuanyi Xue**,[1,2] **and Wangwang Jiang**[1,2]

[1]*College of Mechanical and Vehicle Engineering, Taiyuan University of Technology, Taiyuan 030024, China*
[2]*Shanxi Key Laboratory of Fully Mechanized Coal Mining Equipment, Taiyuan 030024, China*
[3]*School of Mechanical Engineering, Tongji University, Shanghai 201804, China*

Correspondence should be addressed to Xinyu Pang; typangxy@163.com

Received 29 August 2019; Revised 25 December 2019; Accepted 13 January 2020; Published 31 January 2020

Academic Editor: Hyeong Joon Ahn

The shape characteristic of the axis orbit plays an important role in the fault diagnosis of rotating machinery. However, the original signal is typically messy, and this affects the identification accuracy and identification speed. In order to improve the identification effect, an effective fault identification method for a rotor system based on the axis orbit is proposed. The method is a combination of ensemble empirical mode decomposition (EEMD), morphological image processing, Hu invariant moment feature vector, and back propagation (BP) neural network. Experiments of four fault forms are performed in single-span rotor and double-span rotor test rigs. Vibration displacement signals in the X and Y directions of the rotor are processed via EEMD filtering to eliminate the high-frequency noise. The mathematical morphology is used to optimize the axis orbit including the dilation and skeleton operation. After image processing, Hu invariant moments of the skeleton axis orbits are calculated as the feature vector. Finally, the BP neural network is trained to identify the faults of the rotor system. The experimental results indicate that the time of identification of the tested axis orbits via morphological processing corresponds to 13.05 s, and the identification accuracy rate ranges to 95%. Both exceed that without mathematical morphology. The proposed method is reliable and effective for the identification of the axis orbit and aids in online monitoring and automatic identification of rotor system faults.

1. Introduction

A rotor system is a core component of rotating machinery, and the rotor system plays a key role in the stable operation of rotating machinery. Once the rotor system fails, it may cause catastrophic accidents of the whole equipment [1]. Generally, common faults of the rotor system include unbalance, shaft cracks, coupling misalignment, oil whirl, oil whip, rotor-stator rub, rotation stall, and surge. Fault diagnosis by the vibration signal of mechanical equipment is a common and effective method, but vibration signals typically contain a considerable amount of fault information in conjunction with environmental noise. Hence, it is difficult to identify faults by only using vibration signals. Identifying the axis orbit is one of the important methods for fault diagnosis of the rotor system. The axis orbit diagram is composed of two sets of vibration displacement signals, which are perpendicular to each other on the same cross-section. The axis orbit contains a lot of significant information, and the running state of the equipment can be visually and intuitively reflected by the axis orbit diagram. To a certain extent, the intelligent level of fault diagnosis for the rotor system is determined by the automatic identification accuracy of the axis orbit. Therefore, it is of great significance to study the automatic identification of the axis orbit.

In the field of rotating machinery, its fault identification is usually divided into four steps: signal purification, image processing, feature extraction, and automatic identification. There are several methods for signal purification, among which the more common and representative methods include wavelet transform/wavelet packet transform [2–4], harmonic wavelet decomposition, empirical mode decomposition (EMD) [5], and ensemble empirical mode decomposition (EEMD) [6, 7]. Wavelet transform will inevitably cause loss of details when processing signals, and it will also cause problems such as frequency aliasing and threshold selection.

Harmonic wavelet decomposition [8] analyzes arbitrary details in different frequency bands and different decomposition layers and overcomes the problem of loss of details in wavelet decomposition. EMD has good phase retention, but due to the calculation method of EMD decomposition, there are unavoidable problems such as mode aliasing and endpoint effects. Therefore, EEMD has been proposed. This method can well suppress the mode aliasing during the EMD decomposition process. Therefore, EEMD is used in signal purification.

Morphological processing is a method of digital image processing, based on set theory as a mathematical foundation. The basic operations of mathematical morphology include expansion, erosion, opening, and closing. Based on these basic operations, the morphology and structure of digital images can be processed. It has obvious advantages in the invariance and standardization of image translation, rotation, and scaling [9]. The application of the method in image processing of the axis orbit is mainly image purification and data reduction. Compared with traditional signal processing methods, it does not need to know the frequency distribution of noise and required signals in advance and prior knowledge of rotor faults, so it is fast, simple, and efficient.

At present, the commonly used methods of feature extraction include Fourier-Mellin descriptor, geometric parameter methods, and some moment feature extraction methods. The Fourier-Mellin descriptor is a method to describe a closed curve, which is complex and inefficient, and it is only suitable for a single closed curve [10–12]. The geometric parameter method pays attention to the characteristics of the axis orbit graph itself and describes different axis orbit shapes by feature quantization [13]. However, the accuracy of extracting the shape parameters of this method is not high, and when the graph is interfered by large nonlinear noise or the fault features are not obvious, its recognition accuracy will be greatly affected. Moments are operators that describe image features, and they have important applications in the fields of pattern recognition and image analysis. So far, the common moment descriptors can be divided into the following types: geometric moments, orthogonal moments, complex moments, and rotation moments. Among them, the geometric moment was proposed for the earliest time and has a simple form, and its research is the most adequate. The geometric moment is also the called geometric invariant moment because of its invariant features such as rotation, translation, and scaling. Because the Hu invariant moment has a certain description ability for simple image, compared with other operators, it is extremely simple and generally only needs a number to express, so this paper uses the Hu invariant moment as the method of image feature extraction.

With the rapid development of computer technology, intelligent fault diagnosis technology is gradually applied. At present, the widely used methods in the field of rotor system axis orbit feature recognition are the artificial neural network (ANN), support vector machine (SVM), fuzzy clustering, and gray correlation analysis [14–16]. Based on probabilistic neural network (PNN), [17] proposed a feature fusion model and applied it to the automatic identification of the axis orbit of a turbo generator and high-speed centrifugal compressor set. To directly classify the continuous wavelet transform scalogram (CWTS), [18] proposed a novel diagnosis method by using a convolutional neural network (CNN). The BP neural network has the ability of arbitrary complex pattern classification and excellent multidimensional function mapping, has a simple structure, and is of great significance for solving nonlinear complex problems. It has become one of the most widely used neural network models in the world [19]. The fuzzy clustering method is used to cluster and identify the axis orbit of multiple faults in a hydropower station [20], and the gray correlation analysis method is used to automatically identify the axis orbit of water turbine generator units [21]. Some researchers have applied SVM to the fault diagnosis of nuclear power plants, centrifugal pumps, and flow control valves and other equipment [22–24]. The feature extraction and automatic identification of the axis orbit often use invariance pattern identification of its two-dimensional graphics, extract invariance features, and automatically perform identification. Li et al. used the Canny operator and Hu invariant moments to identify the axis orbit in the image discipline and applied artificial fish streamline redundant data and PNN for fault classification [25]. Based on the two-dimensional statistical invariant moments and the Fourier descriptor theory, [26] proposed a technique for extracting the shape characteristics of the axis orbit based on D-S evidence theory information fusion. Zolfaghari et al. used Fourier transform and multilayer perceptron neural network to monitor and classify the broken rotor bar fault [27]. In this paper, a combination of the Hu invariant moment and BP neural network is used to extract and automatically identify the fault signals of the rotor system axis orbit.

Although traditional fault recognition methods can perform filtering, feature extraction, and automatic recognition on fault signals, they do not incorporate mathematical morphology into them, and they have problems of low recognition speed and efficiency. In order to improve this problem, this paper uses mathematical morphology as the image processing method; combines it with EEMD, Hu invariant moment, and BP neural network to process the axis orbit of the rotor system; uses the single-span and double-span rotor test bench to verify the method, which is aimed at improving the speed and efficiency of fault identification in the field of rotating machinery; and provides new research directions and data support for rotor fault diagnosis research.

2. Proposed Method

In the rotor system, the vibration displacement signals of the shafting in two directions are measured, i.e., horizontal direction (X) and vertical direction (Y). The high-frequency noise of the vibration signal is filtered via EEMD. Mathematical morphology is used to optimize the image, and the pure axis orbit is obtained. The Hu invariant moment was calculated and considered as the feature vector. Finally, automatic identification of the axis orbit is realized by the BP neural network. The process of optimization and identification of the axis orbit is shown in Figure 1.

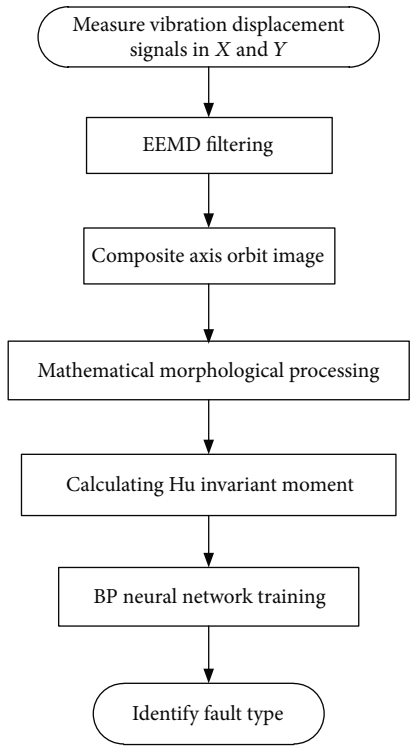

Figure 1: Image optimization and automatic identification process of the axis orbit.

EEMD filtering and image processing make the edge of the axis orbit image smoother and the image structure more concise. This reduces the effort involved in the computation of the image feature vector and improves the calculation efficiency.

2.1. EEMD Filtering. The EEMD exhibits good antimixing filtering properties. White noise is added to the decomposed signal, the mixed signal is evenly distributed in the complete time-frequency space. In the calculation process, a series of Intrinsic Mode Function (IMF) components are obtained by EMD decomposition of signals with the addition of white noise several times. The zero-mean characteristic of white noise is used, and the influence of noise in IMF components is eliminated on average several times, and thus, the effect of suppressing model aliasing is achieved. The EEMD decomposition steps are as follows:

(1) Gaussian white noise $n_i(t)$ with N times mean 0, and an amplitude standard deviation constant is added to the original signal $x(t)$, and this is expressed as

$$x_i(t) = x(t) + n_i(t), \quad i = 1, 2, \cdots, N \tag{1}$$

(2) $x_i(t)$ is decomposed by EMD, and K IMF components and a residual term $r_i(t)$ are obtained:

$$x_i(t) = \sum_{j=1}^{K} c_{ij}(t) + r_i(t). \tag{2}$$

In (2), $c_{ij}(t)$ denotes the jth IMF component after adding Gaussian white noise for the ith time.

(3) Based on the principle that the statistical average value of uncorrelated random sequences is 0, the IMF corresponding to the above steps is conducted in the overall average operation to eliminate the influence of multiple addition of Gaussian white noise on the IMF components. Finally, the IMF components and residual term $r(t)$ after EEMD decomposition are obtained:

$$c_j(t) = \frac{1}{N}\sum_{i=1}^{N} c_{ij}(t), \tag{3}$$

$$r(t) = \frac{1}{N}\sum_{i=1}^{N} r_i(t). \tag{4}$$

In (3), $c_j(t)$ denotes the jth IMF component after the EEMD decomposition of the original signal.

(4) Finally, K IMF components and a residual term are obtained:

$$x(t) = \sum_{j=1}^{K} c_j(t) + r(t). \tag{5}$$

The corresponding low-pass, high-pass, and band-pass filter expressions are obtained through (5). The low-pass filter is expressed as

$$x_{\mathrm{lp}}(t) = \sum_{j=m}^{K} c_j(t) + r(t), \quad 1 < m < K. \tag{6}$$

The high-pass filter is expressed as

$$x_{\mathrm{hp}}(t) = \sum_{j=1}^{n} c_j(t), \quad 1 < n < K. \tag{7}$$

The band-pass filter is expressed as

$$x_{\mathrm{bp}}(t) = \sum_{j=n}^{m} c_j(t), \quad 1 < n < m < K. \tag{8}$$

Simultaneously, the corresponding IMF components are intentionally selected for reconstructing the signal to achieve the filtering effect.

2.2. Mathematical Morphology. The method based on mathematical morphology uses an operator developed by set theory to analyze and process the image [28]. The morphology involves the shape of the image, and this is considered as a set of points. The mathematical morphology defines two basic transformations, namely, image erosion and dilation. The morphological operator is a local transformation that changes the pixel value by defining hit or miss transforms.

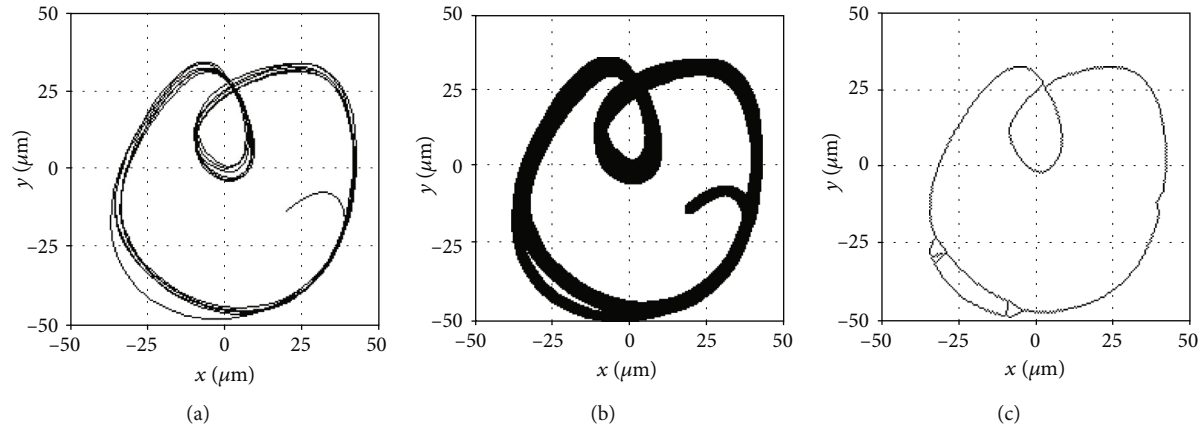

Figure 2: Morphological processing of the axis orbit.

Among them, the pixel value of the image is considered as a set.

In the hit and miss transform, the target of set X is detected by the structural elements of set B, and the processing results for different structural elements on set X are different. The hit or miss transform is defined as follows:

$$X \otimes B = \left\{ x \mid B_x^1 \subset X \cap B_x^2 \subset X^C \right\}. \tag{9}$$

The simplest form of morphological operators is that any one of B^1 or B^2 is empty. When B^1 is empty, Equation (9) is defined as erosion, and Equation (9) corresponds to dilation when B^2 is empty. That is, the processing of image erosion:

$$X \ominus B = \left\{ x \mid B_x^1 \subset X^C \right\}. \tag{10}$$

The processing of image dilation is as follows:

$$X \oplus B = \left\{ x \mid B_x^2 \subset X^C \right\}. \tag{11}$$

The erosion corresponds to a shrinking transformation, and this reduces the gray level of the image. It does not significantly affect the image area with slow changes in the gray level, and it significantly affects the image edge region with evident changes in the gray level. The dilation is an expansion transformation, and this improves the gray level of the image, and it is also sensitive to the image edge region with the evident change of the gray level. The erosion is typically used to filter the interior of the image, and the dilation is generally used to filter the exterior of the image [9, 29].

The image skeletonization is a processing method of image thinning, and this transforms the original image into the image of a few lines (the ideal image is composed of single pixel width lines). The skeleton makes the image more compact. Simultaneously, given the reduction in the effective data, the effort in calculating the image feature vector is reduced, and the computational efficiency improves.

In the study, morphological processing with dilating and skeletonizing is used to deal with the axis orbit as shown in Figure 2. Specifically, Figure 2(a) corresponds to the original image of the axis orbit, and the size is 512×512. The dilated image by using the 6×6 disk structure element is shown in Figure 2(b). The skeleton image is shown in Figure 2(c).

As shown in the results, the original image changes into a clean and clear axis orbit, and the amount of data reduces. This aids in calculating the feature vectors of the axis orbit.

2.3. Hu Invariant Moment for the Image. The moment feature mainly represents the geometric feature of the image, so it is also called the geometric moment. Given its invariant properties of rotating, translating, and scaling, it is also known as the invariant moment. Due to the invariant property of the target moment, the Hu invariant moment theory for image recognition has been proved to have many advantages in feature extraction, and the method is widely used [30, 31].

The invariant moment is similar to the moment of force. It considers the pixel points in the region as a particle and the pixel value as the force arm. The moments are calculated to show the shape characteristics of the region. With respect to a digital image with a size of $M \times N$, its $p+q$ order moments are as follows:

$$M_{pq} = \sum_{i=1}^{M} \sum_{j=1}^{N} i^p j^q f(i,j), \quad p, q = 0, 1, 2, \cdots. \tag{12}$$

In (12), $f(i,j)$ is used as the quality of a pixel, and M_{pq} corresponds to the moment of the image under different p or q. The corresponding $(p+q)$ order central moments are as follows:

$$m_{pq} = \sum_{i=1}^{M} \sum_{j=1}^{N} \left(i - \bar{i}\right)^p \left(j - \bar{j}\right)^q f(i,j). \tag{13}$$

In (13), $(\bar{i}, \bar{j})$ denote the central coordinates of the graph, and $(\bar{i}, \bar{j})$ are calculated as follows:

$$\left(\bar{i}, \bar{j}\right) = \left(\frac{M_{10}}{M_{00}}, \frac{M_{01}}{M_{00}}\right). \tag{14}$$

In order to ensure that the image exhibits invariance of rotation, translation, and scaling, the zero-order central

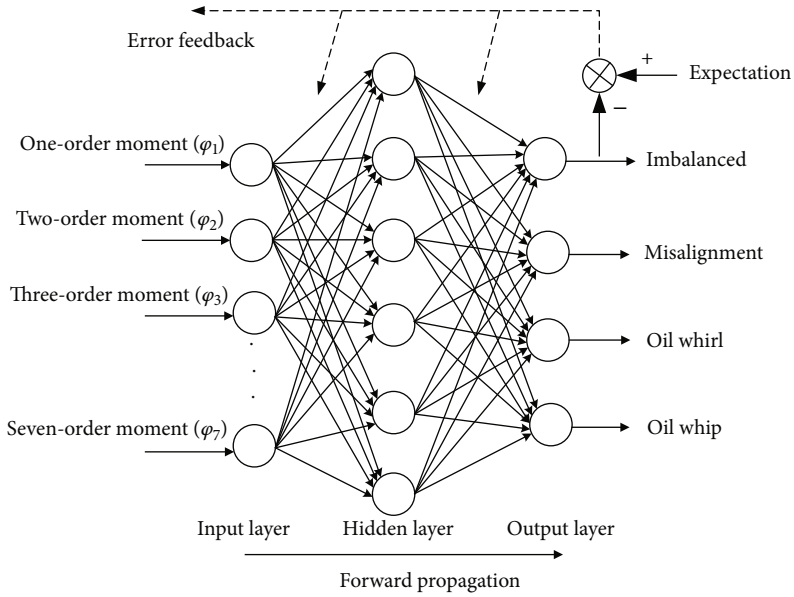

Figure 3: BP neural network topology diagram.

moment is used to normalize the center moment of other orders, and the following normalized central moment is obtained:

$$\mu_{pq} = \frac{m_{pq}}{m_{00}^{\gamma}}, \tag{15}$$

where $\gamma = ((p+q)/2) + 1, p+q = 2, 3, \cdots$.

Using the second and third order normalized central moments, the seven invariant moments are expressed in μ_{pq} with translation, scaling, and rotation invariance:

$$\varphi_1 = \mu_{20} + \mu_{02}, \tag{16}$$

$$\varphi_2 = (\mu_{20} - \mu_{02})^2 + 4\mu_{11}^2, \tag{17}$$

$$\varphi_3 = (\mu_{30} - 3\mu_{12})^2 + (3\mu_{21} - 3\mu_{03})^2, \tag{18}$$

$$\varphi_4 = (\mu_{30} + \mu_{02})^2 + (\mu_{21} + \mu_{03})^2, \tag{19}$$

$$\begin{aligned}\varphi_5 = {} & (\mu_{30} - 3\mu_{12})(\mu_{30} + \mu_{12}) \\ & \cdot \left[(\mu_{30} + \mu_{12})^2 - 3(\mu_{21} + \mu_{03})^2\right] \\ & + (3\mu_{21} - 3\mu_{03})(\mu_{21} + \mu_{03}) \\ & \cdot \left[3(\mu_{30} + \mu_{12})^2 - (\mu_{21} + \mu_{03})^2\right],\end{aligned} \tag{20}$$

$$\begin{aligned}\varphi_6 = {} & (\mu_{20} - \mu_{02})\left[(\mu_{30} + \mu_{12})^2 - (\mu_{21} + \mu_{03})^2\right] \\ & + 4\mu_{11}(\mu_{30} + \mu_{12})(\mu_{21} + \mu_{03}),\end{aligned} \tag{21}$$

$$\begin{aligned}\varphi_7 = {} & (3\mu_{21} - \mu_{03})(\mu_{30} + \mu_{12}) \\ & \cdot \left[(\mu_{30} + \mu_{12})^2 - 3(\mu_{21} + \mu_{03})^2\right] \\ & - (\mu_{30} - 3\mu_{12})(\mu_{21} + \mu_{03}) \\ & \cdot \left[3(\mu_{30} + \mu_{12})^2 - (\mu_{21} + \mu_{03})^2\right].\end{aligned} \tag{22}$$

Among the seven moments of the above equations, the low order moments mainly describe the general features of the image, and the higher order moments mainly describe the detailed features of the image [32]. The invariant moment and the combined moments exhibit a few characteristics that describe the features of the image and are applied in the field of fingerprint identification, scene matching, and chromosome analysis. The Hu invariant moment was used as the feature vector of the axis orbit in this study, and the BP neural network was trained to realize automatic identification by using Hu invariant moments.

2.4. BP Neural Network. The essence of automatic identification of the axis orbit corresponds to the pattern identification of axis orbit images. A neural network is an artificial intelligence technology that establishes a reasoning classification system that simulates the structure of the brain neural network via computers. In the multilayer network structure of a neural network, information is distributed in the weight coefficient of the connection, and this exhibits high fault tolerance and robustness. In the study, the BP neural network used is a multilayer feed-forward neural network. Given that the Levenberg-Marquardt (LM) algorithm exhibits faster convergence speed and higher computing efficiency, the axis orbit identification of the neural network is based on the LM algorithm. Following the determination of the structure of the neural network, the design of the BP network is performed and includes the number of layers, number of neurons, activation functions, initial value, and learning rate of the network. The structure of the BP neural network is shown in Figure 3.

2.4.1. Network Layer. In the study, the one-seven-order Hu moments of the axis orbit are considered as the input to the neural network, and the output is considered as four failure modes (i.e., imbalance, misalignment, oil whirl, and oil whip). The model of the neural network corresponds to a forward feedback type. The structure of the network

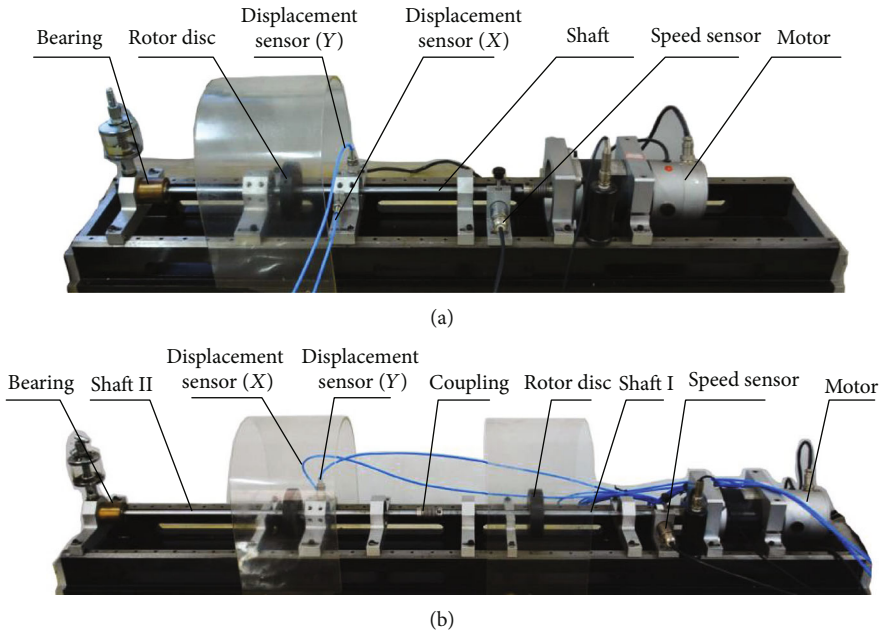

Figure 4: Test rig of rotor system.

contains three layers as follows: input layer, output layer, and hidden layer.

2.4.2. Hidden Layer Node Number. The number of hidden layer nodes should be determined based on the application scenario and precision of the neural network. Under the premise of achieving the requirement of error, a reduction in the number of hidden layer is considered as an improvement.

Based on (23) and the experimental data of the axis orbit, the hidden layer finally contains six nodes as follows:

$$n = \sqrt{n_i + n_o} + a, \tag{23}$$

where n denotes the number of hidden layer nodes, n_i denotes the number of input nodes, n_o denotes the number of output nodes, and a denotes the constant between 1 and 10.

2.4.3. Selection of Initial Weight and Learning Rate. The choice of initial weight significantly affects the training time and determination of convergence. A random number between the initial weight (-1,1) is selected to ensure that the output of each neuron after the initial weighted value is close to zero and that the weight of each neuron is regulated within the maximum range of the sigmoid function.

The learning rate determines the training error and training speed of the neural network. The selection range of the learning rate is between 0.01 and 0.8, and the appropriate learning rate is selected based on the complexity of the identified object.

3. Experiment

3.1. Test Rig. In the study, the rotor system is examined, and experimental data for a single-span rotor and a double-span rotor test rig are collected to verify the applicability and reliability of the identification method in different rotor systems. In identification experiments, training samples are derived from the single-span rotor test rig, and test objects are obtained from the double-span rotor test rig.

Table 1: Speed range of each fault.

Fault types		Speed range (r/min)
Single-span rotor test bench	Unbalance	2716-2861
	Misalignment	1774-2828
	Oil whirl	5917-6231
	Oil whip	7050-7623
Double-span rotor test bench	Unbalance	2511-5530
	Misalignment	1550-1786
	Oil whirl	7575-8010
	Oil whip	8174-8287

The experimental rig corresponds to INV1612 series multifunctional flexible rotor experimental equipment, and this was manufactured by the China Orient Institute of Noise and Vibration. The single-span rotor test rig is shown in Figure 4(a), and its first critical speed is 3120 r/min; the double-span rotor test rig is shown in Figure 4(b), and its first critical speed is 3810 r/min. The horizontal and vertical eddy current sensors are installed near the disk of the rotor test rig. The X direction denotes the horizontal direction, and the Y direction denotes the vertical direction.

The way of setting the misalignment fault is to add a gasket under the bearing pedestal, and the thickness of the gasket is 0.5 mm. Taking the single-span rotor test rig as an example, the misalignment is realized by introducing the offset between the motor and the shaft through the coupling. Specifically, the bearing pedestal close to the motor is raised by 0.5 mm, and the measuring point is near the disc, as shown in Figure 4(a). In order to be consistent with the

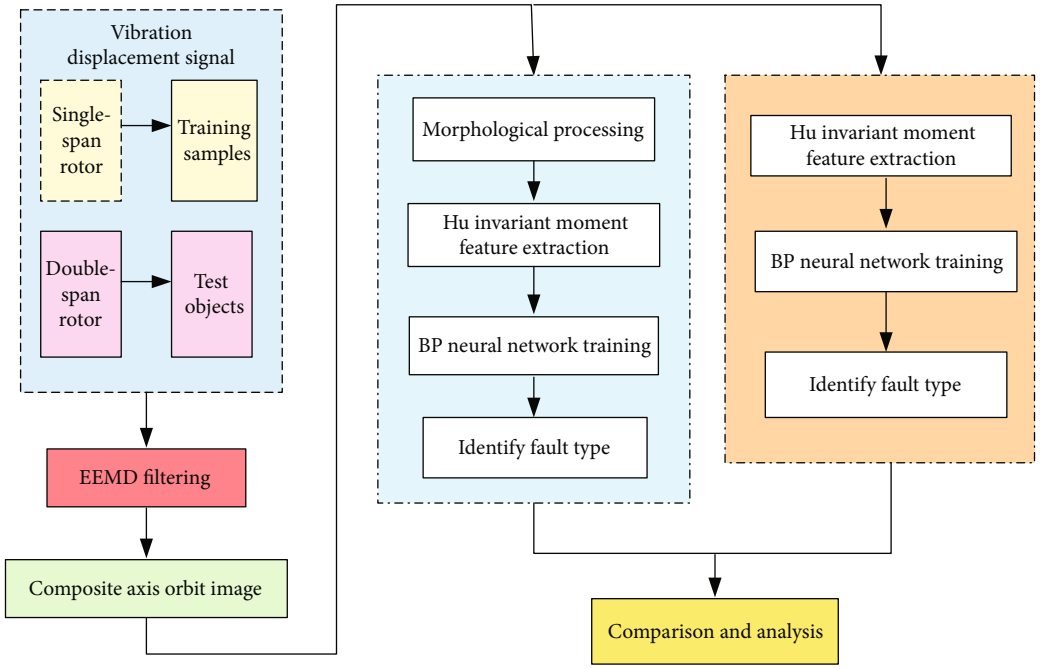

Figure 5: Experimental procedure.

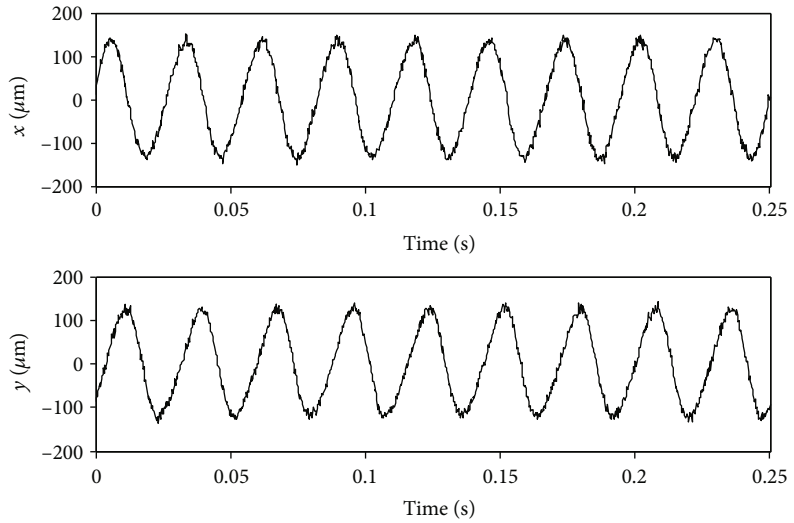

Figure 6: Original axis displacement signal.

single-span measurement point signal, the bearing pedestal in front of the measurement point is also raised 0.5 mm on the double-span rotor to achieve the misalignment. The way to set the unbalance fault is to add a screw in the hole on the disc, and the mass of the screw is 0.5 g.

The speeds corresponding to these four faults (unbalance, misalignment, oil whirl, and oil whip) are shown in Table 1. Because the fault type of the rotor system at low speed is mainly unbalanced and misaligned fault, while the fault of oil whirl and oil whip at high speed is more obvious, the speed corresponding to the imbalance and misaligned fault in this paper is mainly below the first critical speed, while the speed corresponding to oil whirl and oil whip is mainly near the twice critical speed. When collecting sample data on a single-span rotor test rig, the collection time of each fault is 10 s, and the sampling frequency is 4096 Hz, and then, 10 sets of data are randomly arbitrarily intercepted, each set of data contains 512 data points, and the corresponding time is 0.125 s. Based on this, 10 axis orbits under the fault were drawn. In the same way, the test data on the double-span rotor test bench is composed of arbitrarily intercepting 5 sets of data during the collection time of each fault.

As can be seen from Table 1, the speed corresponding to each fault is a range, not a specific value. This is set because the fault image with obvious characteristics can be selected from it, which is convenient for training the model. Compared with determining the speed value, the model has stronger adaptability. In addition, the speed ranges corresponding

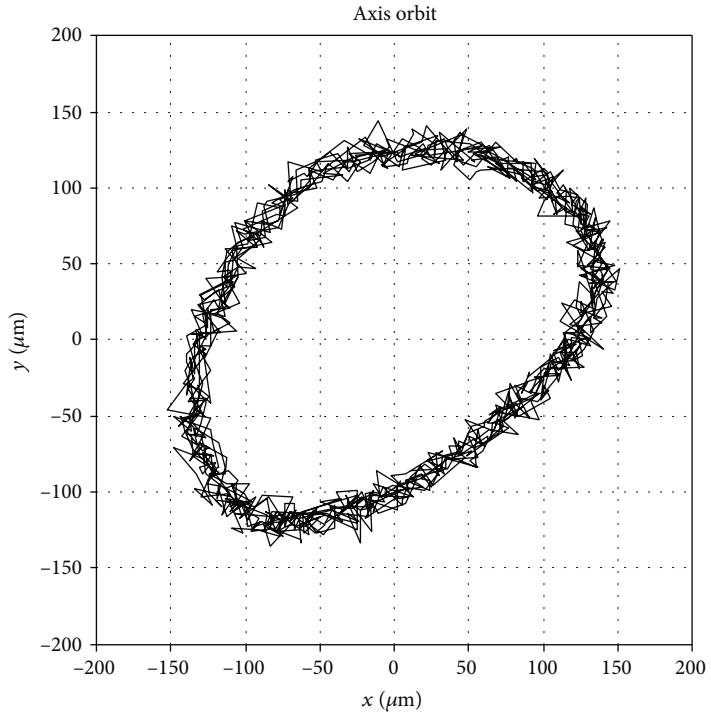

Figure 7: Axis orbit.

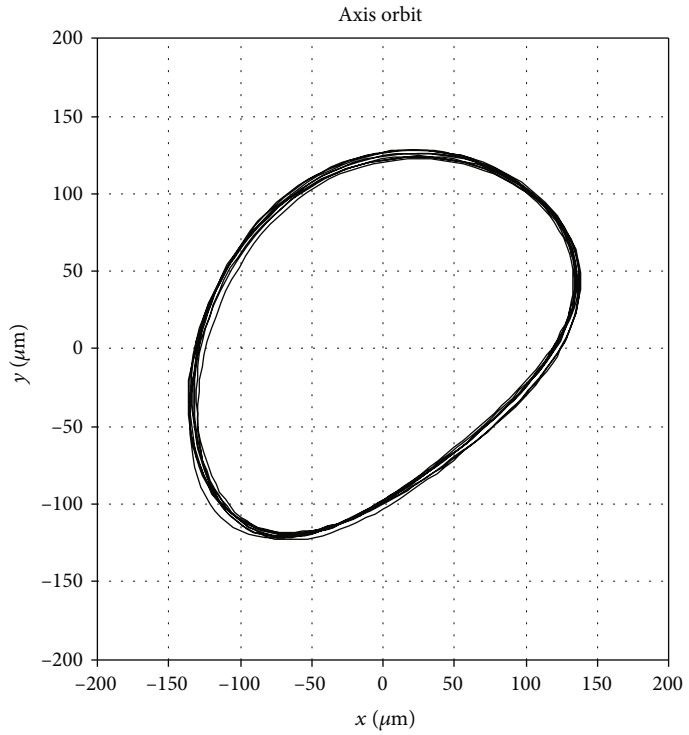

Figure 8: Axis orbit after EEMD processing.

to the same fault types on single-span and double-span rotor test benches are also different. This is to improve the generalization ability of the model, that is, to train the model in one speed range and then apply the model to fault diagnosis in different speed ranges.

3.2. Experimental Plan. In order to reflect the role of mathematical morphology in the pattern identification of the axis orbit, the identification results of the axis orbit with and without morphological processing were compared. The detailed experimental procedure is shown in Figure 5.

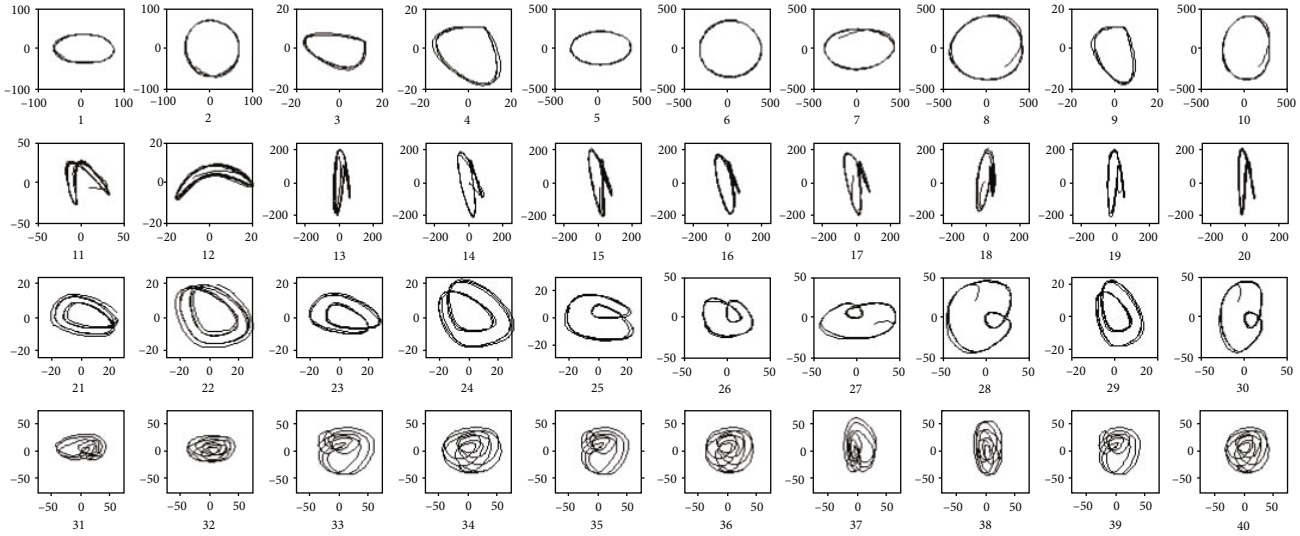

Figure 9: Samples of axis orbits.

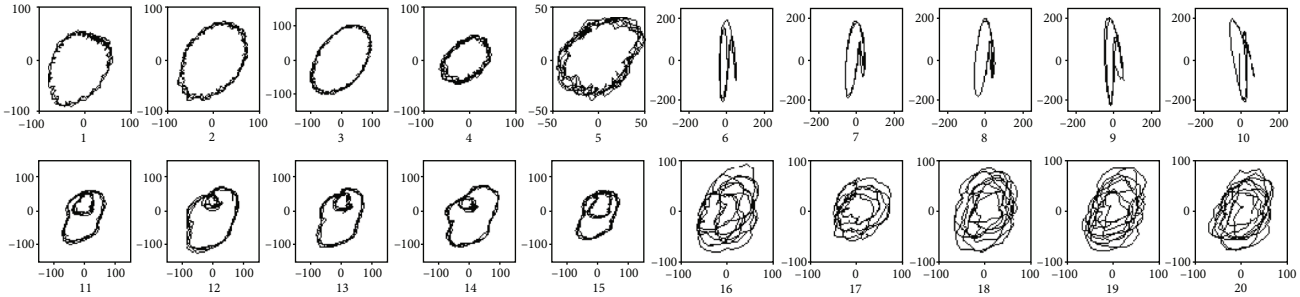

Figure 10: Tested axis orbits.

4. Results and Analysis

4.1. EEMD Filtering Result. The vibration displacement signals in X and Y directions of the rotating shaft in the rotor test rig are shown in Figure 6. Figure 7 corresponds to the axis orbit of the rotor. It is observed that the original signal contains high-frequency vibration noise. The original signal of the axis locus is normalized and filtered via EEMD. The IMF signal component of the noise is removed, and the other IMF signal components are reconstructed. The axis orbit after purification is shown in Figure 8. As shown in Figure 8, the axis orbit image after EEMD filtering is smoother.

4.2. Morphological Processing of the Axis Orbit Image. The vibration displacement signals under four types of faults are collected from a single-span flexible rotor rig. After EEMD filtering and morphological processing, 40 axis orbits are obtained as shown in Figure 9. Among them, the numbers 1-10 represent the imbalanced fault, 11-20 represent the misalignment fault, 21-30 represent the oil whirl fault, and 31-40 represent the oil whip fault.

The 20 axis orbits generated by the double-span flexible rotor rig are used as test objects as shown in Figure 10. Among them, the numbers 1-5 correspond to the imbalanced fault, 6-10 correspond to the misalignment fault, 11-15 correspond to the oil whirl fault, and 16-20 correspond to the oil whip fault.

4.3. Feature Extraction Based on HU Invariant Moments. The Hu invariant moments are calculated based on the image features. The procedure is based on (12), (13), (14), (15), (16), (17), (18), (19), (20), (21), and (22). The Hu invariant moments of the samples are shown in Table 2. The Hu invariant moments of the tested axis orbits are shown in Table 3.

4.4. Parameter Settings of the BP Neural Network. After image processing, the features of the axis orbit are classified by the standard BP neural network. In order to realize the automatic identification of the axis orbit, a BP neural network is established based on the experimental data. The input layer has 7 nodes (Hu invariant moments). The number of hidden layer nodes is 6. The output layer node corresponds to 4. The output coding of the neural network is shown in Table 4. The transfer functions of hidden layer neurons and output layer neurons are *tansig* and *purelim*. The training function and the actual output function of the test sample are *trainlm* and *sim*. The learning rate, maximum epoch, and error goal are set to 0.1, 1000, and 0.001, respectively. Hu invariant moments of samples in Table 2 are used

Table 2: Hu invariant moments of the samples.

Number	Hu invariant moments						
	φ_1	φ_2	φ_3	φ_4	φ_5	φ_6	φ_7
1	1.251	1.829	0.505	-0.897	-1.892	-0.039	-1.056
2	1.337	0.350	1.843	1.907	4.131	1.980	2.453
3	1.165	1.601	2.265	1.231	2.717	1.984	2.130
4	1.169	1.512	2.270	1.741	3.685	2.348	3.204
5	1.286	1.725	0.197	-2.428	-2.294	-1.570	-2.563
6	1.336	1.955	0.271	2.209	3.415	3.185	3.712
7	1.153	1.392	0.802	0.360	1.400	0.745	1.195
8	1.286	0.632	1.139	1.110	1.972	1.365	2.020
9	1.155	1.336	2.286	1.284	3.602	1.951	3.148
10	1.198	1.089	1.100	-0.906	0.026	-0.539	-0.516
11	0.926	1.398	2.440	1.962	4.058	2.500	4.011
12	1.063	1.945	2.734	2.321	4.854	3.007	4.035
13	1.019	1.962	-0.029	-1.255	-1.608	-0.275	-2.479
14	0.917	1.619	1.687	0.987	2.051	-0.439	2.264
15	1.056	2.019	0.721	1.268	2.432	2.271	0.518
16	1.056	1.916	0.814	-0.052	-0.030	0.358	0.149
17	1.063	1.976	0.878	0.444	0.875	1.366	1.051
18	1.035	1.896	0.339	0.511	0.351	1.426	0.935
19	1.042	2.001	0.230	-0.687	-1.848	-0.023	-2.816
20	1.014	1.971	-0.033	-1.111	-1.541	-0.128	-2.323
21	0.706	0.733	-0.253	-0.654	-3.639	-0.537	-1.265
22	0.697	0.369	0.653	-0.193	0.084	-0.736	-0.278
23	0.839	0.966	0.559	-0.246	0.494	-1.322	0.542
24	0.929	1.019	1.334	0.156	0.999	0.125	0.527
25	0.978	1.215	1.684	1.424	3.030	1.770	1.586
26	1.000	0.899	0.942	1.079	2.413	1.523	1.700
27	1.087	1.256	1.173	1.656	3.068	2.184	1.849
28	1.148	0.987	0.594	1.466	1.508	1.706	2.784
29	0.925	0.877	1.368	-0.194	1.012	0.220	0.820
30	1.077	1.365	1.177	1.512	2.962	1.937	2.803
31	0.499	0.405	0.059	0.192	0.317	0.394	-2.003
32	0.507	0.428	-1.133	-1.823	-3.375	-2.117	-4.265
33	0.609	-0.363	-0.529	0.388	0.615	-0.163	0.592
34	0.526	-0.474	-0.801	-0.876	-1.409	-3.416	-1.847
35	0.560	-2.462	-0.511	0.302	0.252	-0.929	0.570
36	0.557	-1.243	-1.058	-1.063	-1.820	-1.686	-1.718
37	0.539	0.372	-0.797	0.041	-0.239	-0.225	0.058
38	0.431	-1.194	-1.643	-2.238	-4.501	-3.082	-3.473
39	0.538	-0.971	-0.309	0.238	-0.699	-0.443	0.568
40	0.537	-0.743	-1.060	-1.198	-2.020	-2.521	-2.005

as feature vectors to train the network. The data in Table 3 is used to test the BP neural network.

4.5. Analysis and Comparison of Identified Results. The neural network output result of the tested axis orbits is obtained via morphological processing and without processing. The output coding of the BP neural network is compared with the output result after rounding, and the fault type of the rotor system is identified.

Table 3: Hu invariant moments of the tested axis orbits.

Number	Hu invariant moments						
	φ_1	φ_2	φ_3	φ_4	φ_5	φ_6	φ_7
1	1.293	1.545	1.728	1.471	2.681	1.671	2.523
2	1.336	1.955	0.271	2.209	3.415	3.185	3.712
3	1.237	1.738	0.647	-0.853	-1.625	-0.198	-0.951
4	1.272	1.314	1.724	1.322	2.651	1.969	3.373
5	1.470	2.190	1.439	1.994	3.890	3.085	3.672
6	0.969	1.871	1.412	1.326	2.774	2.262	2.382
7	1.031	1.914	0.695	-0.836	-0.774	-0.105	-1.241
8	1.041	1.953	0.359	-0.936	-1.683	-0.238	-1.588
9	1.044	2.029	0.231	-0.722	-1.683	-0.094	-1.950
10	1.066	2.005	0.967	-0.073	-1.043	0.373	0.415
11	0.855	0.820	0.981	1.118	2.299	1.292	2.006
12	0.905	1.002	1.160	1.281	2.513	1.667	0.633
13	0.998	1.183	1.345	1.519	2.450	1.712	2.966
14	1.067	0.954	1.311	1.139	2.404	1.612	2.918
15	0.998	1.175	1.442	1.425	3.267	2.010	2.345
16	0.521	-0.089	-0.342	-0.913	-1.198	-0.958	-1.005
17	0.643	-0.837	0.486	-0.642	-0.228	-1.394	-1.182
18	0.649	0.128	-0.238	-0.859	-1.352	-0.817	-2.135
19	0.571	0.040	0.217	-0.861	-1.558	-1.379	-2.149
20	0.402	-0.426	-0.890	-1.462	-3.135	-1.817	-2.574

Table 4: Expected outputs of the forward feedback neutral network.

Fault type	Output 1	Output 2	Output 3	Output 4
Imbalance	0	0	0	1
Misalignment	0	0	1	0
Oil whirl	0	1	0	0
Oil whip	1	0	0	0

Table 5: Comparison of the tested axis orbits by morphological processing and without processing.

Processing mode	Time of training and identification	Identification accuracy rate
Morphological processing	13.054 s	95%
Without morphological processing	16.827 s	80%

The comparison of the tested axis orbits by morphological processing and without processing is shown in Table 5. The training and identifying time of the BP neural network of tested axis orbits by morphological processing is 13.054 s, and this is less than the time in the without processing condition. The identification accuracy rate is 95%, and this exceeds that in the without processing condition.

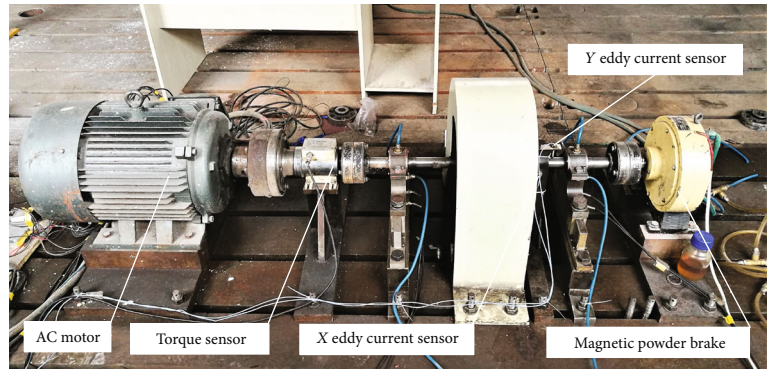

Figure 11: Rotor rig for testing.

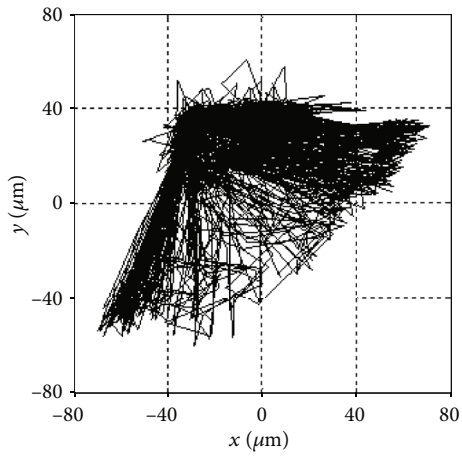

Figure 12: Axis orbit of original signals.

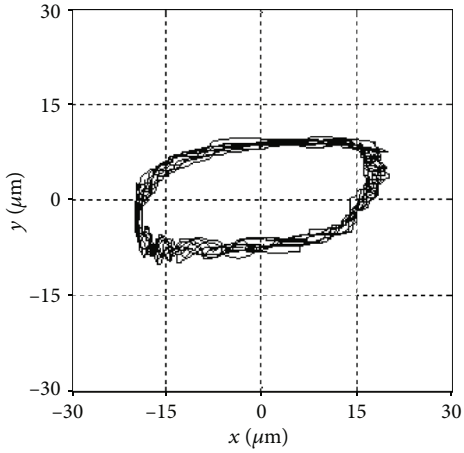

Figure 13: Axis orbit after filtering.

5. An Application Example

In order to further verify the effectiveness of the autorecognition fault method of the morphological processing axis orbit, the experiment was carried out through another self-designed rotor test rig, that is, a single-disc flexible rotor system. The test rig is shown in Figure 11. The axis orbit was generated by axial displacement signals from X and Y eddy current sensors. A certain amount of imbalance was set in the disc to verify the recognition result.

Due to noise interference in the original signal, the axis orbit is very messy, as shown in Figure 12. In this paper, the original signals were processed by median filtering. The axis orbit after filtering is shown in Figure 13.

It can be seen that the filtered signal becomes smoother. However, the edge of the axis orbit is still messy, which is disadvantageous to recognition of fault. The dilated image and the skeleton image of the axis orbit were obtained by a series of mathematical morphological processing, as shown in Figures 14 and 15.

The Hu invariant moments of the skeleton axis orbit in Figure 15 are shown in Table 6. The neural network output results are shown in Table 7. The result of Table 7 shows that the rotor test rig has imbalanced fault. It is proved that this method can realize automatic recognition.

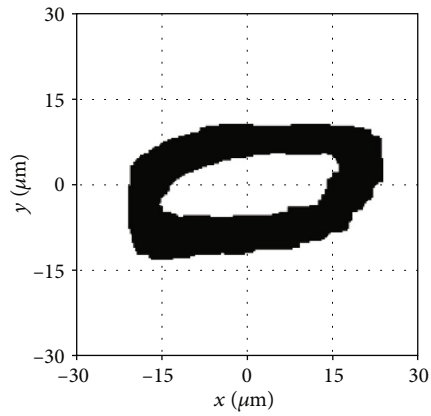

Figure 14: Dilated image of axis orbit.

6. Conclusions

Morphological processing played an important role in the automatic identification of an axis orbit. The axial

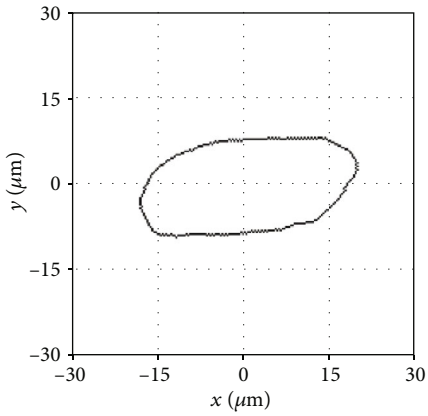

Figure 15: Skeleton image of axis orbit.

Table 6: Hu invariant moments of the verified axis orbit.

φ_1	φ_2	φ_3	φ_4	φ_5	φ_6	φ_7
1.248	1.430	2.346	0.961	2.919	1.035	3.459

Table 7: Neural network output result of the verified axis orbit.

Output results				Fault type
-0.001	-0.001	0.003	1.004	Imbalance

displacement signals were filtered by EEMD to eliminate high-frequency noise, and the image of the axis orbit was then processed by using mathematical morphology including the dilation and skeleton operation. The axis orbit is adequately restored by the method.

In the study, Hu invariant moments of the skeleton axis orbits were calculated, and the BP neural network was trained by using the Hu invariant moment as the feature vectors to identify the fault. In the experiment, 40 samples were trained, and 20 axis orbits were tested. The results indicate that the calculation speed is evidently improved. Additionally, the identification accuracy rate is up to 95%, and this exceeds that without using mathematical morphology.

The method solves the problem of automatic identification of the fault in the actual working conditions. It is a reliable and effective method for identifying the axis orbit. The use of the axis orbit for fault diagnosis of the rotor system has a good practical value, which is conducive to debugging and online monitoring of the rotor system.

Data Availability

The data used to support the findings of this study are included within the article.

Conflicts of Interest

The authors declare that there are no conflicts of interest regarding the publication of this paper.

Acknowledgments

The financial support from National Nature Science Foundation of China (NSFC) (51805352) and Natural Science Foundation of Shanxi Province (201901D111062).

References

[1] C. Wang, *Research and Application of Digital Image Processing and Analysis in Fault Diagnosis*, Huazhong University of Science and Technology, 2012.

[2] A. Hernández, C. Castejón, J. C. García-Prada, I. Padrón, and G. N. Marichal, "Wavelet packets transform processing and genetic neuro-fuzzy classification to detect faulty bearings," *Advances in Mechanical Engineering*, vol. 11, no. 8, 2019.

[3] D. Zhen, Z. Wang, H. Li, H. Zhang, J. Yang, and F. Gu, "An improved cyclic modulation spectral analysis based on the CWT and its application on broken rotor bar fault diagnosis for induction motors," *Applied Sciences*, vol. 9, no. 18, p. 3902, 2019.

[4] Y. Zhang, X. du, G. Wen, X. Huang, Z. Zhang, and B. Xu, "An adaptive method based on fractional empirical wavelet transform and its application in rotating machinery fault diagnosis," *Measurement Science and Technology*, vol. 30, no. 3, article 035005, 2019.

[5] P. Singh and S. P. Harsha, "Statistical and frequency analysis of vibrations signals of roller bearings using empirical mode decomposition," *Proceedings of The Institution of Mechanical Engineers, Part K: Journal of Multi-Body Dynamics*, vol. 233, no. 4, pp. 856–870, 2019.

[6] Y. Shrivastava and B. Singh, "Online monitoring of tool chatter in turning based on ensemble empirical mode decomposition and Teager filter," *Transactions of the Institute of Measurement and Control*, 2019.

[7] Y. Cheng, Z. Wang, B. Chen, W. Zhang, and G. Huang, "An improved complementary ensemble empirical mode decomposition with adaptive noise and its application to rolling element bearing fault diagnosis," *ISA Transactions*, vol. 91, pp. 218–234, 2019.

[8] S. Li, "Harmonic wavelet packetes method and used on accurate obtaining the orbit of rotor sub-frequency signal," *Chinese Journal of Mechanical Engineering*, vol. 40, pp. 133–137, 2004.

[9] S. Sha and G. Weng, "Purification of shaft orbit with mathematical morphology filters," *Journal of Soochow University (Engineering Science Edition)*, vol. 27, pp. 39–41, 2007.

[10] J. Zhang and S. Fu, "Shape recognition based on fourier descriptor of moments," *Microcomputer Information*, vol. 34, pp. 167–169, 2009.

[11] B. Fu, J. Zhou, W. Chen, and Y. Binghui, "A method based on Fourier descriptors to recognize shaft orbit," *Automation of Electric Power Systems*, vol. 28, pp. 40–44, 2004.

[12] Y. Wang, M. Liao, and B. Wu, "Automatic identification of the axis oribt shape of a rotor," *Mechanical Science and Technology for Aerospace Engineering*, vol. 27, pp. 799–803, 2008.

[13] H. Wang and R. Zhao, "Fault feature extraction method of rotor system based on combination of fractal and geometrical characteristics," *Noise and Vibration Control*, vol. 34, pp. 166–170, 2014.

[14] A. Jawadekar, S. Paraskar, S. Jadhav, and G. Dhole, "Artificial neural network-based induction motor fault classifier using

continuous wavelet transform," *Systems Science & Control Engineering*, vol. 2, no. 1, pp. 684–690, 2014.

[15] A. T. Jahromi, M. J. Er, X. Li, and B. S. Limb, "Sequential fuzzy clustering based dynamic fuzzy neural network for fault diagnosis and prognosis," *Neurocomputing*, vol. 196, pp. 31–41, 2016.

[16] F. Xu, B. Zhong, and R. Huang, "Automatic recognition of shaft orbit and its application to fault diagnosis of rotating machinery," *Journal of Vibration, Measurement and Diagnosis*, vol. 29, pp. 141–145, 2009.

[17] Q. Jiang, Y. Shen, H. Li, and F. Xu, "New fault recognition method for rotary machinery based on information entropy and a probabilistic neural network," *Sensors*, vol. 18, no. 2, p. 337, 2018.

[18] S. Guo, T. Yang, W. Gao, and C. Zhang, "A novel fault diagnosis method for rotating machinery based on a convolutional neural network," *Sensors*, vol. 18, no. 5, p. 1429, 2018.

[19] P. Liu and W. Zhang, "A fault diagnosis intelligent algorithm based on improved BP neural network," *International Journal of Pattern Recognition and Artificial Intelligence*, vol. 33, no. 9, article 1959028, 2019.

[20] H. Li, L. Bai, X. Luo, J. Rong, and T. Lulin, "Multi-fractal feature recognition for shaft centerline orbit of hydropower units based on fuzzy clustering," *Journal of Hydroelectric Engineering*, vol. 31, pp. 238–242, 2012.

[21] Y. Li and Q. Chen, "Automatic identification of axis orbit of hydroelectric generating set based on grey theory and moment invariants," *Automation of Electric Power Systems*, vol. 25, pp. 19–22, 2001.

[22] H. Wang, M. J. Peng, J. Wesley Hines, G. Y. Zheng, Y. K. Liu, and B. R. Upadhyaya, "A hybrid fault diagnosis methodology with support vector machine and improved particle swarm optimization for nuclear power plants," *ISA Transactions*, vol. 95, pp. 358–371, 2019.

[23] J. S. Rapur and R. Tiwari, "Multifault diagnosis of combined hydraulic and mechanical centrifugal pump faults using continuous wavelet transform and support vector machines," *Journal of Dynamic Systems, Measurement, and Control*, vol. 141, no. 11, article 111013, 2019.

[24] S. K. Venkata and S. Rao, "Fault detection of a flow control valve using vibration analysis and support vector machine," *Electronics*, vol. 8, no. 10, p. 1062, 2019.

[25] Q. Li, W. Wang, and X. Liu, "Intelligent recognition of axis orbits with fish-based algorithms and neural networks with mentors," *Journal of Hydroelectric Engineering*, vol. 34, pp. 191–196, 2015.

[26] L. Zhao, *Investigation on Failure Mechanism and Shift Orbits Recognition Methods for Rotating Machine*, Dalian University of Technology, 2010.

[27] S. Zolfaghari, S. Noor, M. Rezazadeh Mehrjou, M. Marhaban, and N. Mariun, "Broken rotor bar fault detection and classification using wavelet packet signature analysis based on Fourier transform and multi-layer perceptron neural network," *Applied Sciences*, vol. 8, no. 1, p. 25, 2018.

[28] M. S. Nixon and A. S. Aguado, *Feature Extraction and Image Processing*, Academic Press, 2010.

[29] N. S. Vyas and D. Satishkumar, "Artificial neural network design for fault identification in a rotor-bearing system," *Mechanism and Machine Theory*, vol. 36, no. 2, pp. 157–175, 2001.

[30] D. F. Shi, W. J. Wang, P. J. Unsworth, and L. S. Qu, "Purification and feature extraction of shaft orbits for diagnosing large rotating machinery," *Journal of Sound and Vibration*, vol. 279, no. 3-5, pp. 581–600, 2005.

[31] X. Yonggang, M. Hailong, F. Mingshi, and C. Lingli, "New method for weak signal detection based on invariant moment," *Journal of Vibration, Measurement & Diagnosis*, vol. 32, pp. 568–571, 2012.

[32] Y. Qian, H. Zhang, D. Peng, and F. Xia, "Orbit purification of generator units based on a new generalized particle swarm optimization method," *Proceedings of the Chinese Society of Electrical Engineering*, vol. 32, pp. 130–137, 2012.